Biomedicine & Pharmacotherapy 202 (2026) 119832

Contents lists available at ScienceDirect

Biomedicine & Pharmacotherapy

journal homepage: www.elsevier.com/locate/biopha

Trametinib-mediated MEK inhibition impairs cancer cell viability and invasion in patient-derived tumor avatars of glioblastoma with extraneural metastases: A proof-of-concept study

Metka Novak [a,b,1], Bernarda Majc [a,1], Marija Skoblar Vidmar [c,h,1], Špela Kladnik [a], Tina Kolenc Milavec [a,d], Anamarija Habič [a,d], Simona Katrin Galun [a,d], Pia Žižek [a,d], Andrej Porčnik [e], Alenka Matjašič [f], Andrej Zupan [f], Miha Jerala [f], Matic Bošnjak [f], Borut Prestor [e], Barbara Breznik Vittori [a,g,*]

[a] National Institute of Biology, Department of Genetic Toxicology and Cancer Biology, Ljubljana 1000, Slovenia
[b] Biotechnical Faculty, University of Ljubljana, Ljubljana 1000, Slovenia
[c] Institute of Oncology Ljubljana, Ljubljana 1000, Slovenia
[d] Jožef Stefan International Postgraduate School, Ljubljana 1000, Slovenia
[e] Department of Neurosurgery, University Medical Centre Ljubljana, Ljubljana 1000, Slovenia
[f] Institute of Pathology, Faculty of Medicine, University of Ljubljana, Ljubljana 1000, Slovenia
[g] Faculty of Chemistry and Chemical Technology, University of Ljubljana, Ljubljana 1000, Slovenia
[h] Faculty of Medicine, University of Ljubljana, Ljubljana 1000, Slovenia

ARTICLE INFO

Keywords:
Glioblastoma
Extraneural metastasis
Rare clinical case
Organoids
MEK inhibitor
Cancer stem cells
Cell invasion

ABSTRACT

Glioblastoma (GBM) remains one of the most lethal human malignancies, yet extraneural metastases are exceptionally rare and poorly understood. Standard treatment—surgical resection followed by chemoradiotherapy—offers only modest survival benefits, and therapeutic options for metastatic GBM are limited. Here, we describe a rare clinical case of metastatic GBM and provide comprehensive molecular characterization alongside a potential targeted treatment strategy. The tumor exhibited several molecular features associated with aggressive behavior, including alterations in the tumor suppressor genes *NF1, TP53, PTEN*, and *RB1*, a mesenchymal DNA-methylation subclass, and activation of the MAPK signaling pathway. To functionally evaluate therapeutic vulnerabilities, we developed tumor models using patient-derived GBM cells and their assembloids with cerebral organoids that recapitulate patient-specific tumor biology and the human brain microenvironment. We identified the MEK inhibitor trametinib as a promising candidate capable of selectively reducing viability and invasion of highly aggressive, stem-like GBM cells within our personalized patient-derived tumor avatars. This work highlights the proof-of-concept evidence that MEK pathway inhibition may represent a potential therapeutic vulnerability to counteract rapid tumor spread and improve responsiveness to temzolomide in this individual metastatic GBM case. Study underscores the need for continued research to advance targeted, multi-modal therapeutic approaches for GBM.

1. Introduction

Glioblastoma (GBM) remains one of the most lethal human cancers, with a median overall survival of only 14–16 months despite standard-of-care treatment consisting of maximal safe surgical resection followed by radiotherapy and chemotherapy with the DNA-alkylating agent temozolomide (TMZ) [1]. Current therapeutic strategies have achieved only limited success, largely because they fail to address the extensive

* Corresponding author at: National Institute of Biology, Department of Genetic Toxicology and Cancer Biology, Ljubljana 1000, Slovenia.
E-mail addresses: metka.novak@nib.si (M. Novak), bernarda.majc@nib.si (B. Majc), mskoblar@onko-i.si (M.S. Vidmar), Spela.Kladnik@nib.si (Š. Kladnik), Tina.Kolenc.Milavec@nib.si (T.K. Milavec), Anamarija.Habic@nib.si (A. Habič), SimonaKatrin.Galun@nib.si (S.K. Galun), Pia.Zizek@nib.si (P. Žižek), andrej.porcnik@kclj.si (A. Porčnik), alenka.matjasic@mf.uni-lj.si (A. Matjašič), andrej.zupan@mf.uni-lj.si (A. Zupan), miha.jerala@mf.uni-lj.si (M. Jerala), matic.bosnjak@mf.uni-lj.si (M. Bošnjak), borut.prestor@kclj.si (B. Prestor), barbara.breznik@nib.si (B.B. Vittori).
[1] Shared first authorship

https://doi.org/10.1016/j.biopha.2026.119832
Received 21 June 2026; Received in revised form 25 July 2026; Accepted 1 August 2026
Available online 4 August 2026

heterogeneity of GBM. This heterogeneity contributes to incomplete treatment responses and rapid development of resistance through adaptive phenotypes and dynamic rewiring of multiple signaling pathways in cancer cells [2].

Extraneural metastasis of GBM is exceedingly rare, occurring in only 0.4–0.5% of patients, with the lungs, pleura, lymph nodes, bone marrow, bone, and liver being the most commonly affected sites [3]. The mechanisms enabling GBM cells to disseminate beyond the central nervous system remain poorly understood. The detection of circulating tumor cells exhibiting mesenchymal (MES) gene signature suggests that this phenotype may facilitate metastatic spread [4–6]. A deeper understanding of the biological processes underlying GBM metastasis is essential for identifying potential preventive and therapeutic targets.

GBM is characterized by highly infiltrative growth and resistance to therapy, driven by activation of multiple intracellular signaling pathways, including the transforming growth factor beta (TGF-β) [7,8], focal adhesion kinase (FAK) [9], and mitogen-activated protein kinase/extracellular signal-regulated kinase (MAPK/ERK) [10]. These pathways have emerged as promising therapeutic targets for gliomas. Several MEK inhibitors are already FDA-approved for other malignancies, such as melanoma, non–small cell lung cancer and NF−1 mutation-associated benign peripheral nerve sheath tumors, although preclinical and clinical data in GBM remain limited [10–12]. Trametinib (TRA), an oral selective MEK1/2 inhibitor approved for the treatment of patients (pediatric and adults) with melanoma, non-small cell lung cancer, and anaplastic thyroid cancer with BRAF V600E or V600K mutations, is capable of crossing the blood–brain barrier [11]. FAK inhibitors have shown encouraging results in preclinical GBM models, enhancing the effects of TMZ and prolonging survival in animal models [13,14]. Similarly, the TGF-β receptor I inhibitor galunisertib (GAL) has demonstrated anti-tumor activity in GBM animal models [15].

Although numerous preclinical studies have demonstrated encouraging antitumor effects, no durable clinical benefits have yet been achieved in randomized trials involving patients with GBM. This gap highlights the need for more physiologically relevant preclinical models that can accurately capture the complexity, heterogeneity, and biological behavior of human GBM and better predict therapeutic efficacy. Advanced 3D culture systems—such as tumor spheroids and organoids—more closely recapitulate tumor architecture, the heterogeneous tumor microenvironment, nutrient and oxygen gradients, and metabolic conditions, thereby now emerging as a translationally useful platform for mirroring clinical responses to therapy [16–18]. Human healthy brain organoids assembled with GBM spheroids or organoids (called assembloids or hybrid organoids) enable assessment of both on-tumor efficacy and off-tumor safety within a brain-like microenvironment [19,20].

In this proof-of-concept evidence study, we describe a rare clinical case of GBM with extraneural metastases and perform extensive molecular characterization of tumor biopsies. Our primary aim was to evaluate the preclinical efficacy of targeted therapy and inhibitors targeting signaling pathways associated with aggressive GBM phenotypes using advanced *in vitro* models. These included patient-derived cell cultures, as well as cerebral organoid-GBM assembloids generated as personalized tumor avatars. Additionally, we sought to optimize cerebral organoid culture conditions and monitoring tumor cell invasion in assebloids, with the goal of facilitating future testing of anti-invasive strategies for GBM.

2. Materials and methods

2.1. Ethics statements

Approval by the National Medical Ethics Committee of the Republic of Slovenia was obtained (number 0120–190/2018–2711–46) for collecting and processing tumor tissue material, performing research on patient's material, and using the corresponding personal data. Patient or their authorized representatives signed the informed consent form in accordance with the Declaration of Helsinki.

2.2. Patient and tumor tissue collection

Female patient of age 47 was enrolled into the study after her diagnosis with GBM. Diagnosis, imaging and treatment were performed according to standard clinical procedures at the University Medical Center Ljubljana and the Institute of Oncology, Ljubljana, Slovenia.

Resected tumor tissue was obtained from the Department of Neurosurgery at the University Medical Centre Ljubljana, Slovenia. Immediately after surgical resection, the tumor tissue was transported to the Institute of Pathology at the Faculty of Medicine, University of Ljubljana, Slovenia, for histopathological and molecular examination, and National Institute of Biology, Slovenia, for storage and research analysis. Fresh tumor tissue was used to establish primary GBM cell lines that were stored in GlioBank [21]. Procedures for collecting and storing biological material were developed in accordance with best practice guidelines.

2.3. Histopathological and molecular evaluation of tumor

Histopathological evaluations of tumor and biopsies were performed based on standard clinical procedure at the Institute of Pathology at the Faculty of Medicine, University of Ljubljana and Institute of Oncology Ljubljana, Slovenia. GBM diagnosis was determined using the standard histopathology and molecular protocols at the Institute of Pathology of the Medical Faculty, University of Ljubljana based on the latest WHO classification 2021 [22].

2.4. Tumor tissue enrichment and DNA/RNA extraction

Molecular analyses were performed on primary and recurrent tumors. DNA and RNA were extracted from formalin-fixed paraffin-embedded (FFPE) tissue after tumor enrichment using 0.6-mm punch sampling of areas with > 60% tumor cellularity, as assessed by a neuropathologist and molecular pathologist. Nucleic acids were isolated using the Maxwell RSC DNA Plus FFPE or RNA FFPE kits (Promega) with overnight proteinase K digestion. DNA/RNA quantity and quality were assessed using NanoDrop One and Qubit 3.0 (Thermo Fisher Scientific).

2.5. Next generation sequencing analyses

Prior to library preparation, DNA samples were treated with uracil-DNA glycosylase (UDG) enzyme. Libraries were prepared using the Oncomine Comprehensive Assay (OCA; Thermo Fisher Scientific) covering hotspot variants, indels, copy number variations, and gene fusions across 161 unique genes (for the OCA panel gene list, visit Oncomine Comprehensive Assay v3M at www.thermofisher.com). We used 15 ng of UDG-treated DNA and 50 ng of total RNA. Library preparation was performed according to the manufacturer's instructions. Libraries were quantified, pooled, and sequenced on the Ion S5 system following template preparation on the IonChef instrument (Thermo Fisher Scientific). Sequencing data were processed using Torrent Suite and analyzed in Ion Reporter software with GRCh37/hg19 as the reference genome. Manufacturer-provided workflows were used for variant detection, annotation and tumor mutation burden assessment.

2.6. Tumor methylation profiling

Genome-wide DNA methylation profiling of the primary tumor was performed using the Illumina Infinium HumanMethylationEPIC (850 K) array. Bisulfite-converted DNA was hybridized to arrays, scanned on the Illumina iScan system, and analyzed using the Brain Tumor Classifier (v12.5) for tumor classification, which performs quality control, normalization, and unsupervised clustering based on reference brain

tumor methylation classes.

2.7. GBM cell culture

Primary GBM cells and GSCs have been established from the same tumor region but distinct parts of the recurrent tumor specimen at the time of second surgery. For isolation of primary GBM cells NIB315, fresh recurrent GBM tumor biopsies were minced with scalpels in high-glucose Dulbecco's modified Eagle's medium (DMEM) (Hy-clone, GE Healthcare) supplemented with 10% fetal bovine serum (FBS; Gibco, Thermo Fisher Scientific), 2 mM L-glutamine, and 1 × penicillin/streptomycin (both Sigma-Aldrich) and were seeded in six-well cell culture plates (Corning). Growing cells were detached with a 0.25% trypsin–EDTA solution (Gibco) and transferred to T25 or T75 cell culture flasks (Corning). Cells were passaged in this manner at least three times and expanded for subsequent analysis and storage purposes.

For isolation of GSCs NIB315, tissue pieces of recurrent GBM tumor biopsies were digested in a digestion buffer (200 U/mL collagenase II and collagenase IV (both Gibco) in Neurobasal Medium (Invitrogen, Life Technologies). Cell suspensions were filtered using a cell strainer with 100 μm pores (BD Falcon, Corning). Single cells were harvested and resuspended in complete Neurobasal Medium containing 2 mM L-glutamine, 1 × penicillin/streptomycin (both Sigma-Aldrich), 1 × B−27 (Invitrogen), 1 U/mL heparin (Sigma-Aldrich), 20 ng/mL basic fibroblast growth factor (bFGF) and epidermal growth factors (EGF) (both Invitrogen). GSCs were cultured as floating spheres in an untreated cell culture flask (Sarstedt Inc.). Once these GSC spheres reached a diameter of 200 μm, they were dissociated using TrypLE Express (Gibco) and expanded for subsequent analysis and storage purposes.

Cell cultures were checked for Mycoplasma using MycoAlert Mycoplasma Detection Kit (Lonza).

2.8. Human induced pluripotent stem cells (iPSC)

Human induced pluripotent stem cells (iPSCs) (Cellular Dynamics International, Inc.; CW60441EE1) were obtained from SciLifeLab (Stockholm, Sweden) at passage 16 and used for experiments between passages 19 and 23. iPSCs were routinely cultured on Matrigel® hESC-qualified matrix (Corning)–coated 6-well plates (Corning). Cells were maintained in mTeSR™1 Basal Medium supplemented with 1 × mTeSR™1 Supplement (STEMCELL Technologies). For passaging, ReLeSR™ (STEMCELL Technologies) was used according to the manufacturer's instructions. Culture medium was refreshed every other day. Cells were cryopreserved using mFreSR™ (STEMCELL Technologies) following the manufacturer's protocol.

2.9. Cell lysis and protein quantification

Cells were harvested, washed with 1x PBS and pelleted using mini-centrifuge. Cell pellets were resuspended, and cells were lysed in RIPA lysis and extraction buffer (Thermo Fisher Scientific) supplemented with Halt™ Protease Inhibitor Cocktail (Thermo Fisher Scientific) and Halt™ Phosphatase Inhibitor Cocktail (Thermo Fisher Scientific). Suspension was incubated on ice for 15 min and subsequently centrifuged 15 min at 13.000 rpm and 4 °C (Micro 200 R, Hettich Labinstrument AB). Protein concentration was determined using Pierce™ BCA Protein Assay Kit (Thermo Fisher Scientific). All samples were analyzed in two replicates. For standardization curve, bovine serum albumin in concentrations from 2 mg/mL to 10 mg/mL was used. All samples were diluted 1:24 in dH2O, 1x RIPA was used for background removal. After 30 min incubation at 37 °C absorbance at 576 nm was measured with Synergy Spectrophotometer (Bio Tek). Concentrations of the samples were calculated based on the standard curve equation.

2.10. Western blotting

Samples of 25 μg of proteins were used for western blot profiling. Samples were prepared by mixing protein extract with NuPAGE® LDS Sample Buffer (Thermo Fisher Scientific), NuPAGE® Reducing Agent (Thermo Fisher Scientific) and deionized water to the total volume of 30 μL, followed by heat denaturation (10 min, 70 °C). Proteins were separated for 1 h at 180 V on 4–12% polyacrylamide Bis-Tris gels with MES running buffer (all reagents from NuPAGE®, Thermo Fisher Scientific). Proteins were transferred onto methanol-activated Immobilon®-FL PVDF Membrane (Merck) using iBlot™ 2 Dry Blotting System (Invitrogen) according to manufacturer instructions. Membranes were blocked in Intercept Blocking Buffer TBS (Licor) for 1 h and probed overnight at 4 °C with primary antibodies: anti phospho-FAK Y397 (ab81298, 1:1000), anti FAK (sc−1688, 1:200), anti phospho-MEK1/2 S217/221 (cs−9154, 1:1000), anti MEK1/2 (cs−9122, 1:1000) and anti TGFBR1 (ab235578, 1:1000), diluted in Intercept antibody diluent (Licor). Anti β-Tubulin (Licor 926–42211, 1:1000) or anti GAPDH (ab9485, 1:1000) antibody were used as loading controls. After washing for three times 5 min in PBS-T: 1x PBS (Thermo Fisher Scientific) with 0,2% Tween20 (Thermo Fisher Scientific), membranes were probed with secondary antibodies IRDye 800CW Goat Anti-Rabbit IgG (H+L) (Licor, 925–32211, 1:15.000) or IRDye 680RD Goat Anti-Mouse IgG (H+L) (Licor, 925–68070, 1:15.000) for 1 h in the darkness while gently shaking. After washing in PBS-T buffer 3 × 5 min, resulting signals were visualized on the Odyssey® Sa Infrared Imaging System (Licor) and quantified using Empiria Studio 3.2 software. Raw western blot images and corresponding densitometric quantification data have been deposited in a public data repository [23]. Graphs and statistical analyses were generated using GraphPad Prism 10.

2.11. Cell viability assay

Cell viability was assessed using the 3D Cell Viability Assay CellTiter-Glo® (Promega) after 48 h and 1 week of treatment. Three small-molecule inhibitors were used for treatment: GAL, TRA and VS−4718, with the following final concentrations for each inhibitor: 1 μM, 5 μM, and 10 μM for GAL; 50 nM, 100 nM, and 200 nM for TRA; and 150 nM, 300 nM, and 600 nM for VS−4718. Dimethyl sulfoxide (DMSO) (0,2%, 0,3%, 0,4%) was used as vehicle control. For the adherent (GBM) cell line, 100 μl of media was removed from each well of the 96-well plate, and 100 μl of CellTiter-Glo® Reagent was added to each well and mixed, followed by a 10-min incubation on a shaker in the dark at room temperature (RT). After incubation, the entire volume from each well was transferred to a 96-well white flat-bottom microplate (Corning®) and incubated for another 20 mins in the dark at RT. After 20 min, luminescence was measured using a Synergy HTX plate reader. For the suspension (GSC) cell line, 100 μl of cell suspension from each well of the 96-well plate was immediately transferred to a white flat-bottom microplate (Corning®). Then, 100 μl of CellTiter-Glo® Reagent was added to each well, and the contents were mixed, followed by a 10-min incubation on a shaker, then removed from the shaker and incubated for another 20 min in the dark at RT. Then, luminescence was measured using a Synergy HTX plate reader. Cerebral organoids (COs) were treated with 200 nM TRA, 100 μM TMZ, or their combination (50 nM TRA + 100 μM TMZ). For the CO cell viability assay, 100 μl of media was removed from each well of the 96-well plate, and 100 μl of CellTiter-Glo® Reagent was added to each well containing an CO and mixed vigorously, followed by a 10-minute incubation on a shaker in the dark at RT. After incubation, the entire volume from each well was transferred to a 96-well white flat-bottom microplate (Corning) and incubated for another 20 min in the dark at RT. After 20 min. Luminescence was then measured using a Synergy HTX plate reader. Graphs and statistical analyses were generated using GraphPad Prism 10.

2.12. Cell cytotoxicity assay

Cell cytotoxicity was assessed using the LDH-Glo™ Cytotoxicity Assay (Promega) according to the manufacturer's instructions after 48 h and 1 week of treatment. Three small-molecule inhibitors were used to treat GBM and GSC cell lines: GAL, TRA and VS−4718, with final concentrations of each inhibitor: 1 μM, 5 μM and 10 μM for GAL; 50 nM, 100 nM and 200 nM for TRA; and 150 nM, 300 nM and 600 nM for VS−4718. Cerebral organoids were treated with 200 nM TRA, 100 μM TMZ, or their combination (50 nM TRA + 100 μM TMZ). DMSO (0,2%, 0,3%, 0,4%) was used as vehicle control. Cell-conditioned medium from each well was diluted 1:2.5 in LDH Storage Buffer and dispensed in triplicate into clear Corning® 384-well Low Flange White Flat Bottom Polystyrene TC-treated Microplates (Corning). The LDH detection reagent was added at a 1:1 (v/v) ratio to each well, followed by a 45 min incubation at RT, after which luminescence was measured using a Synergy HTX plate reader. Graphs and statistical analyses were generated using GraphPad Prism 10.

2.13. 3D Matrigel invasion assay

A 3D Matrigel invasion assay was performed on GSC spheroids prepared using anti-adherence rinsing solution. A 96-well plate (Falcon) was pre-treated with 25 μL of anti-adherence rinsing solution (STEMCELL Technologies) per well for 10 min at RT. The solution was then removed, and the wells were washed once with PBS. After removing PBS, the plates were allowed to dry completely at RT. After plate preparation, 5000 NIB315 GSCs per well were seeded into the plate. The plate was centrifuged for 10 min at 300 rpm to promote cell settling. After centrifugation, the plate was incubated for 2 days to allow spheroids to form well-defined spheres. Five different conditions were tested with the following final concentrations: control, 0.2% DMSO, TRA 10 nM, TRA 10 nM + TMZ 100 μM, and TMZ 100 μM. The volume of Matrigel (Corning® Matrigel® Basement Membrane Matrix) was calculated according to the number of wells for each condition to reach a final concentration of 30%. 100 μL of Matrigel solution in media with or without treatment was added to each well of a U-bottom non-treated 96-well plate (Falcon), followed by transfer of spheroids to each well using wide-bore pipette tips. After transferring all spheroids, images of all wells were acquired using the EVOS M7000 Imaging System (Thermo Fisher Scientific) with a 4 × objective under brightfield illumination. Invasion was monitored for 1 week, and images were acquired on days 1, 4, and 7. Quantification of invasion was performed using ImageJ. Graphs and statistical analyses were generated using GraphPad Prism 10.

2.14. Cerebral organoid (CO) generation

Cerebral organoids were generated based on a published protocol [21] with modifications to improve long-term survival. Briefly, on day 1, human iPSCs at ~80% confluency were dissociated into single cells and seeded into ultra-low attachment round-bottom 96-well plates (Corning) at 40,000 cells per well in PSC Neural Induction Media (NIM; Gibco) supplemented with 4 ng/mL bFGF (Gibco) and 20 μM Y−24632 Rock inhibitor (Abcam).

On day 2, successful embryoid body (EB) formation was confirmed; EBs appeared as round clusters with translucent borders. On day 4, the medium was replaced with fresh NIM. On day 7, the medium was refreshed with NIM lacking bFGF and Y−27632. On day 10, EBs were transferred to the Celvivo ClinoStar system (Celvivo) and cultured in Brain Organoid Medium containing 50% DMEM/F12 (Thermo Fisher Scientific), 50% Neurobasal Media (Thermo Fisher Scientific), 1 × penicillin/streptomycin (Sigma-Aldrich), N−2 supplement (Thermo Fisher Scientific), B−27™ Supplement (Gibco), Human Insulin (Merck), 2-Mercaptoethanol (Thermo Fisher Scientific), GlutaMAX (Gibco), MEM Non-essential Amino Acids Solution (Thermo Fisher Scientific) and bFGF (Gibco). Rotational speed was adjusted according to organoid size to ensure optimal conditions. Organoids were maintained in the ClinoStar system for over 3 months for further applications.

Day 1 was defined as the initiation of EB formation. CO (e.g., day 40, 3 months) refers to the time elapsed since day 1. For co-culture experiments with NIB315 GSC spheroids and for immunofluorescence analyses, CO at day 40 of differentiation were used.

2.15. Flow cytometry

Assessment of the expression of CO cell type–specific markers after three months in culture was performed by flow cytometry. COs were dissociated into a single-cell suspension by gentle enzymatic digestion using the Tumor Dissociation Kit (Miltenyi Biotec) according to the manufacturer's instructions. For the live/dead assay, cells were stained with 7-AAD (Miltenyi Biotec) for 5 min. For cell-type marker analysis cells were fixed in 4% buffered formaldehyde (Merck) for 10 min at RT, washed, and permeabilized for 10 min in 0,1% Triton X−100 (Sigma-Aldrich) in 1 × PBS containing 2% FBS. Cells were then washed, resuspended in 1 × PBS containing 2% FBS, and stained with primary antibodies: anti-SOX2 (ab171380, 1:50; neural stem/progenitor cells), anti-beta III Tubulin (TUJ1) (ab78078, 1 μg/mL; early immature neurons), anti-MAP2 (ab11267, 2 μg/mL; late immature neurons), anti-NeuN (MAB377, 1:125; mature neurons), anti-GFAP (ab211271, 1:1000; astrocytes), anti-EAAT1 (ab416, 1:200; astrocytic marker), anti-OTX2 (MA5–15854, 1:200; forebrain/midbrain identity) and anti-PAX6 (ab195045, 1:200; dorsal forebrain/neural progenitor identity) for 30 min at 4 °C. After washing with 1 × PBS containing 2% FBS, cells were incubated with Alexa Fluor 647–conjugated goat anti-mouse (A21236, 1:200) and goat anti-rabbit (A21244, 1:200) secondary antibodies for 30 min at 4 °C, washed, and analyzed on an Attune NxT Acoustic Focusing Cytometer (Thermo Fisher Scientific). Data were analyzed using the FlowJo software (BD Life Sciences).

2.16. GSC staining

To investigate treatment effects, we generated co-cultures of COs and GSC spheroids (CO–GSC assembloids). GSC spheroids were prepared as described in the 3D Matrigel invasion assay section. On the day of co-culture preparation, GSC spheroids were transferred into 1 mL of Neurobasal medium (without supplements) for staining. 1 μL of CellTracker™ Orange CMTMR Dye (Thermo Fisher Scientific) was added. The spheroids were incubated for 1 h at 37°C to allow for dye uptake, with gentle mixing every 10 min to ensure even labeling. After staining, spheroids were washed with PBS to remove excess dye.

2.17. CO-NIB315 GSC assembloid (hybrid organoid) formation, cytotoxicity, and invasion assay

For assembloids, one CO and one fluorescently stained GSC spheroid were placed together in each well of a 96-well plate and incubated for 24 h at 37°C and 5% CO_2 to ensure fusion between the CO and the spheroid, forming CO-NIB315 GSC assembloids. After 24 h, treatment was initiated with four tested conditions in the following final concentrations: control, 0.2% DMSO, TRA 50 nM and TRA 50 nM + TMZ 100 μM. For the 1-week of treatment, therapy was added three times in 48 h intervals, and cell cytotoxicity was measured after 7 days of treatment. Treated CO-NIB315 assembloids were then fixed in 4% buffered formaldehyde (Merck) for 72 h at 4°C and embedded in 1% agarose in PBS. The agarose blocks were dehydrated and paraffin-embedded, after which 4-μm FFPE sections were prepared for immunofluorescent staining.

2.18. Immunofluorescent staining

Formalin-fixed, paraffin-embedded sections on slides were

deparaffinized in xylene (Chem-Lab) and rehydrated through a series of ethanol solutions (Merck). Antigens were retrieved by heating in 10 mM sodium citrate buffer (pH 6.0) at 95℃ for 20 min. CO (day 40 and 3 month) and assembloid sections were blocked for 1 h at RT in 10% normal goat serum (Sigma-Aldrich), 0.1% Triton X−100 (v/v) and 1% BSA (w/v) (both Sigma-Aldrich) in 1 × PBS. Primary antibodies anti-SOX2 (ab171380, 1:50; neural stem/progenitor cells), anti-βIII-tubulin (TUJ1; ab78078, 1 μg/mL; early immature neurons), anti-NeuroD1 (ab60704, 1:200; early immature neurons), anti-MAP2 (ab11267, 2 μg/mL; late immature neurons), anti-NeuN (MAB377, 1:500; mature neurons), anti-GFAP (ab211271, 1:1000; astrocytes), anti-EAAT1 (ab416, 1:250; astrocytic marker), anti-OTX2 (MA5–15854, 1:200; forebrain/midbrain identity) and anti-PAX6 (ab195045, 1:350; dorsal forebrain/neural progenitor identity), anti-Ki67 (ab15580, 1:1000; proliferating cells), anti-carbonic anhydrase IX (CA9; ab243660, 1:200; hypoxia marker), and anti-CD133 (ab19898, 1:100; GSC marker), diluted in 1% BSA (w/v) in 1 × PBS, were applied to the sections and incubated overnight at 4 °C in a humidified chamber. After washing with 0.5% BSA, slides were incubated with Alexa Fluor 488 goat anti-rabbit secondary antibody (A11008; 1:200) for 1 h at RT in a humidified chamber. The slides were subsequently washed with 1 × PBS, and nuclei were stained with Hoechst 33258 (Sigma-Aldrich; 1:1000 in 1 × PBS) for 5 min at RT. Following a final PBS wash, slides were mounted with ProLong™ Glass Antifade Mountant (Invitrogen), coverslipped, and sealed with nail polish.

2.19. Fluorescence and confocal microscopy

Widefield fluorescence scan images were acquired with EVOS M7000 Imaging System (Thermo Fisher Scientific) with the accompanying software (Diamond Scope, Thermo Fisher scientific). For fluorescence detection, the EVOS™ Light Cube DAPI and EVOS™ Light Cube GFP LED light cubes were used to visualize nuclei and Alexa Fluor 488-labeled markers, respectively, using a 20 × /0.75 Plan Apo CC objective.

Confocal images were acquired using a Leica STELLARIS 8 microscope and LAS X software Version 4.5.0.25531 (Leica Microsystems). A 405 nm laser was used for nuclear staining, and the white light laser was tuned to 495 nm for excitation of Alexa Fluor 488–labeled markers. Emission was collected at 420–486 nm for nuclear signals and 500–789 nm for Alexa Fluor 488, using a 20 × /0.7 UV objective.

2.20. Image analysis

Cell invasion of NIB315 GSCs into COs was analyzed with Celleste 6 Image Analysis Software (Thermo Fisher Scientific). For image analysis, smart segmentation was first applied to define background versus green fluorescent signal (CD133 staining), generating binary masks of the fluorescent regions. The area of the segmented green signal was then quantified as uncalibrated area (in pixels) for each image. The measured green fluorescent signal area was then normalized to the total area of the CO–NIB315 assembloid in each image. Four CO assembloids per condition were used as biological replicates. For each biological replicate, six consecutive sections were analyzed as technical replicates. All raw fluorescence images used for this analysis are publicly available in a data repository [23]. Graphs and statistical analyses were generated using GraphPad Prism 10. Data were plotted as column graphs and nested graphs using GraphPad Prism 10.

2.21. Statistics

The statistical analyses were performed using GraphPad Prism 10. Statistical differences between groups were assessed using ordinary one-way ANOVA with Dunnett's multiple comparisons test, and nested one-way ANOVA with Dunnett's multiple comparisons test was used for experiments with multiple technical measurements nested within biological replicates. Welch's t-test was used for western blot quantification for the comparisons between GBM and GSC cell lines. All data are presented as mean±SEM. The p-values are indicated in the figures as follows: *$p < 0.05$; **$p < 0.01$; ***$p < 0.001$ and not statistically significant if $p > 0.05$ (no asterisk).

3. Results

3.1. Clinical case presentation of glioblastoma with extraneural metastases

Clinical data and timeline are presented in Fig. 1. The patient presented with headache, right sided hemianopsy and Gerstman syndrome. First magnetic resonance imaging (MRI) showed around 4.5 cm big heterogenic rim-enhancing mass with surrounding edema. Tumor showed broad attachment to the dura (Fig. 2A). An operation was performed where subtotal resection was achieved. Tumor was attached to the dura and was mostly well demarcated from the surrounding brain as meningioma. However, towards the occipital horn of the ventricle the tumor grew infiltrative and here some of 5-ALA positive tumor remained. Postoperative MRI shoved a small 15 mm remnant towards the ventricle (Fig. 2A). Symptoms improved and the patient was referred to the oncological treatment. The patient was initially in good general condition following the first oncological evaluation at 1 month after surgery. Blood tests were within normal limits, and there were no reported symptoms such as headache or pain. Based on pathohistological and molecular genetic findings (GBM, IDH-wt, no methylation on MGMT promoter) the oncology multidisciplinary team recommended treatment according to the Stupp's protocol, which includes concurrent radiotherapy and TMZ chemotherapy, followed by adjuvant TMZ chemotherapy. Radiotherapy planning was performed using contrast-enhanced CT simulation in combination with MRI simulation. Patient immobilization was achieved using a thermoplastic mask system. A VMAT (Volumetric Modulated Arc Therapy) technique was used for treatment planning and delivery. MRI and CT images were fused for precise target delineation. Gross Tumor Volume (GTV) included the resection cavity visualized on gadolinium-enhanced T1-weighted MRI sequences. Clinical Target Volume (CTV) encompassed areas at risk for microscopic disease spread and was defined as GTV + 1.5 cm. Planning Target Volume (PTV) was generated by adding an additional 0.4 cm margin to the CTV to account for patient movement and setup variability during treatment delivery (Fig. 2B). The patient completed radiotherapy. Due to thrombocytopenia (a common side effect of TMZ), TMZ was discontinued during the last two fractions of radiotherapy. Treatment resumed with a reduced TMZ dose of 100 mg daily on a 7 days on /7 days off schedule.

After the third adjuvant cycle, the patient experienced clinical deterioration, including severe headaches and vomiting. MRI findings confirmed extensive progression of the disease. MRI showed radiological recurrence of the tumor. There was one tumor the size of 5 cm in resected area and another one of size 5 cm nearby, both showing dural attachment. On the upper edge of tentorium there was another tumor, a few millimeters in size, mimicking meningioma (Fig. 2A). Gross total removal of bigger tumors was performed. The tumor of a few millimeters on tentorium remained. The intraoperative consistency of both tumors and their strong attachment to the dura mimicked the meningioma. Pathohistological findings after second surgery confirmed mitotically active and predominantly vital GBM recurrence, with only 30% of radiation necrosis present in the resection specimen of the tumor bed. After the second operation, the patient's performance status (WHO PS 2) declined, with clinical signs including psychomotor slowing and unilateral (left eye) visual impairment. Second-line chemotherapy with lomustine was initiated. Due to the history of bicytopenia, the dose was reduced to 75% of standard. However, after 1 month, the patient was urgently admitted to the Oncology Institute Ljubljana due to systemic weakness and chest pain. A CT scan revealed widespread metastatic disease, involving the liver, lungs, and skeletal system (Fig. 2C). This

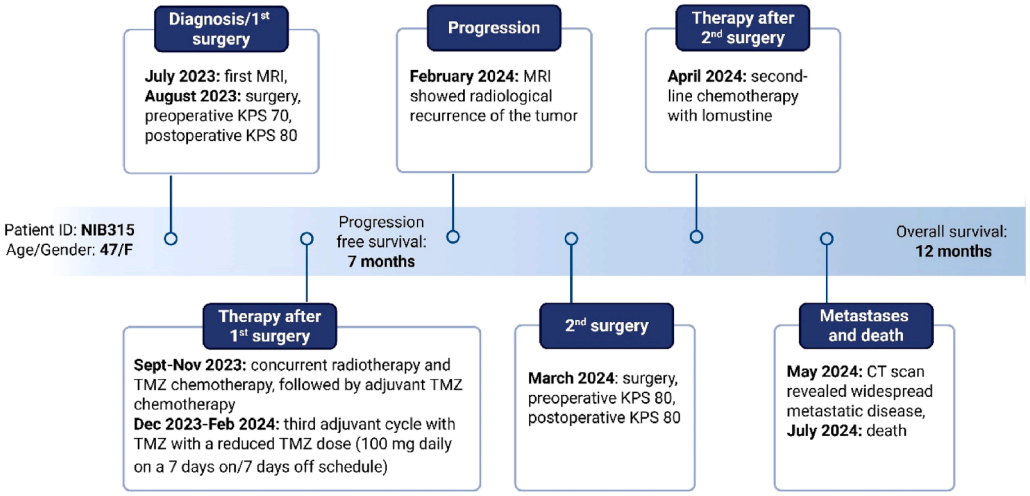

Fig. 1. Clinical data and timeline.

was further confirmed by cytological analysis, which demonstrated extracranial metastases of GBM. Following this, patient condition deteriorated rapidly: she became immobile, experienced dysphagia and with significant bone pain. Following her hospitalization in a terminal condition, during which she was noted to be actively dying, she subsequently passed away.

3.2. *Histopathological and molecular-genetic evaluation of tumor biopsies*

Histopathological tumor evaluation (Fig. S1A) showed that the primary tumor was cellular, with epithelioid and spindled cells, with rare pleomorphic giant and multinucleated cells. Mitotic count index reached 8/mm^2. There was infiltrative growth at the periphery of the tumor, endothelial proliferation as well as abundant areas of tumor necrosis. The tumor at the time of the second surgery (Fig. S1B) had similar morphology, but a higher proportion of spindled and pleomorphic cells as well as more prominent myxoid and collagenous stroma in the background. The tumor invaded the surrounding brain matter in the form of sharply demarcated tongue-like projections as opposed to the more typical infiltrative growth observed in the primary tumor.

Molecular analysis of primary tumor revealed non-methylated MGMT promotor and multiple clinically relevant genetic alterations (Table 1). A pathogenic TERT promoter mutation (c.–124C>T, C228T) was detected at low allele frequency, consistent with telomerase activation. Several tumor suppressor genes showed inactivating alterations, including PTEN (frameshift with premature stop), RB1 (frameshift), TP53 (pathogenic missense variant), and NF1 (nonsense mutation), all present at high allele frequencies, indicating clonal events. An additional ARID1A missense variant of uncertain significance was also identified. Copy number analysis demonstrated high-level amplifications on chromosome 7, involving EGFR, MET, CDK6, BRAF, and PMS2, as well as a broader chromosome 7 gain. Additional chromosomal alterations included amplification of chromosome arm 3p and chromosome 9, while no copy number changes were detected at CDKN2A/CDKN2B, 10q, or 19q. No gene fusions were identified.

The relapse retained the core mutational profile of the primary tumor (Table 1), supporting clonal continuity. However, it showed a marked reduction in copy number alterations, particularly the absence of chromosome 7 amplifications seen in the primary tumor.

Methylation profiling (EPICv2, FFPE) classified the primary tumor as the adult type GBM, IDH-wild-type with a calibrated score of 0.99, and predicted the subclass as GBM, IDH-wild-type, mesenchymal type (0.99).

Ultrasound-guided fine needle aspiration biopsy of liver metastasis was microscopically examined, and immunocytochemistry was performed. Cellular, polymorphic pattern in which there are large tumor cells with basophilic cytoplasm and one or more hyperchromatic nuclei were shown. Blood was seen in the background. Immunocytochemical reactions were negative for epithelial marker CKAE3/AE3, astrocytic marker GFAP, neuronal marker NFp, melanocytic marker Melan A, ambiguous for melanocytic markers HBM45 and melanoma cocktail marker panel, and strongly positive for neuroectodermal marker S100, implicating poorly differentiated GBM metastatic cells in liver.

1. MEK and FAK signaling pathways are activated and TGF-β receptor is expressed in GBM cells

Following recurrent tumor resection at the time of second surgery and tissue processing to establish GBM cell line that was serum grown and had differentiated cell phenotype [21] as well as GSC cell lines that was grown as neurospheres in serum-free conditions (Fig. S2). The patient was designated as NIB315 and was subsequently enrolled in the GlioBank [21] for *in vitro* analyses. As MEK/ERK (MAPK), FAK, and TGF-β signaling are frequently aberrantly activated in GBM, we first profiled the baseline activation of these pathways in NIB315 GBM and GSC cell lines using western blot analysis of total and phosphorylated pathway components (Fig. 3). This enabled us to select the most relevant small-molecule inhibitors for further investigation. Western blot analysis confirmed the expression of Transforming Growth Factor Beta Receptor 1 (TGFBR1) in both GBM and GSC cell lines, identifying it as a potential target for GAL, a TGFβRI small-molecule inhibitor. FAK was expressed in all tested cell lines, with phosphorylation at Tyr397 (pFAK Y397) detected in high levels in GSCs, indicating active FAK signaling alongside activation of the MEK signaling pathway, as shown by the expression of MEK1/2 and phosphorylated MEK1/2 (pMEK1/2 S217/221) in both GBM and GSC cell lines. Accordingly, VS−4718, an inhibitor of FAK, and TRA, a MEK1 and MEK2 inhibitor, were also selected for this study (Fig. 3A). No significant differences in the expression of tested proteins between GBM and GSC cell lines were observed (Fig. 3B).

2. MEK inhibitor trametinib decreases cell viability of GBM and GSC cell lines

Based on the confirmed expression and activation of MEK/ERK, FAK, and TGF-β pathway components, we proceeded to test the effects of their respective small-molecule inhibitors and their combination with TMZ on NIB315 GBM and GSC cell lines. To evaluate the inhibitory effect of each compound, NIB315 cell lines were treated with multiple concentrations of GAL, TRA, and VS−4718 for 48 h and 1 week (Fig. 4, Fig. S3). A

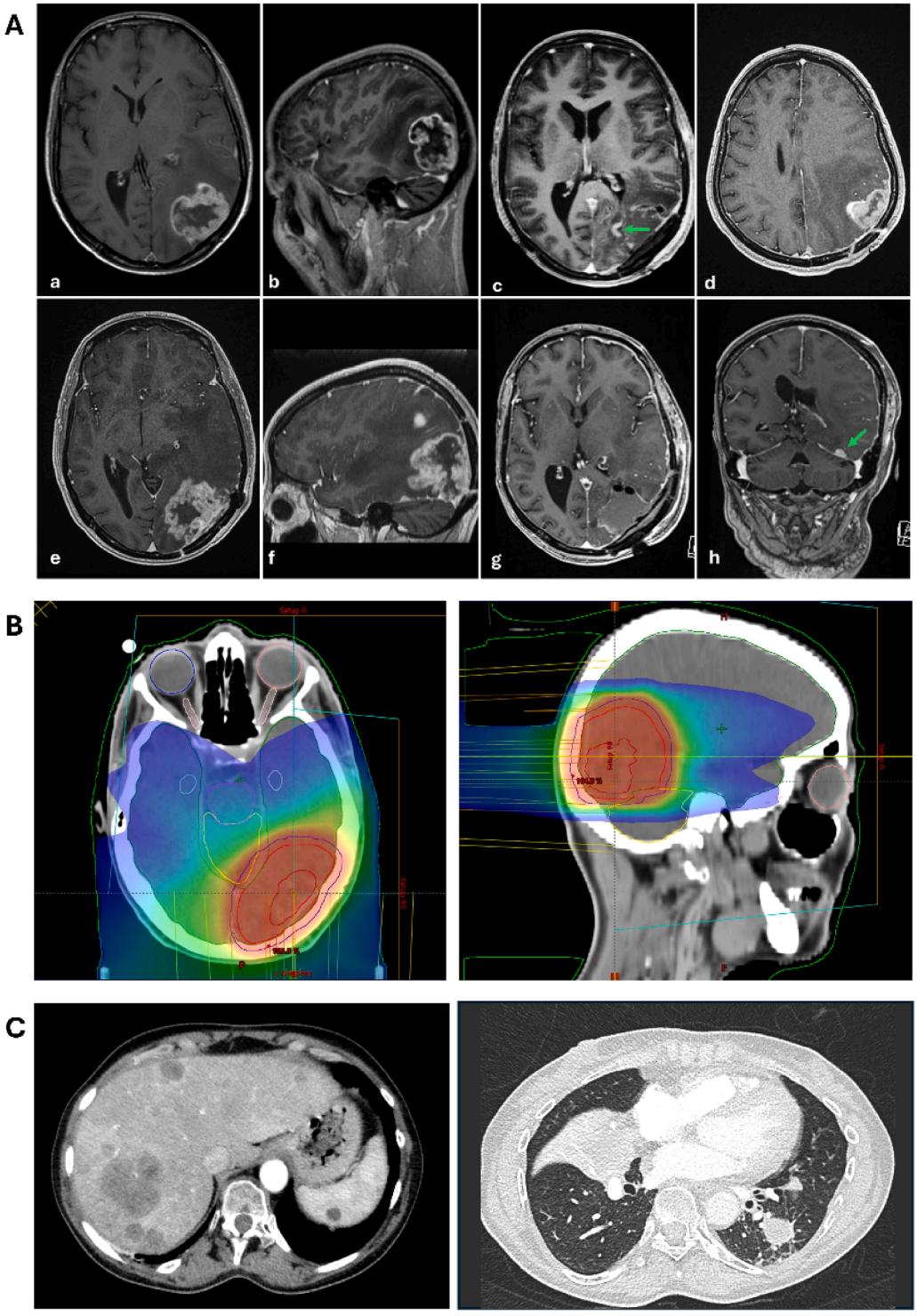

Fig. 2. A (a-h) MRI scans. There is rim-enhanced GBM (a and b) with central necrosis and broad attachment to the dura. Magnetic resonance imaging after the first operation (c) shows a small tumor remnant (arrow). Magnetic resonance imaging 7 months after the operation (d, e and f) showed 3 tumors, all attached to the dura. A gross total resection was achieved after the second operation (g), only one small "meningioma-like" tumor remained on the tentorium (arrow in h). (B) Volumetric Modulated Arc Therapy (VMAT): Gross Tumor Volume (GTV) includes resection cavity seen on MRI T1 with gadolinium; Clinical Target Volume (CTV) includes areas at risk for microscopic disease spread GTV + 1. 5 cm, Planning Target Volume (PTV) CTV plus an additional margin 0.4 cm to account for patient movement and setup variability. (C) A contrast-enhanced computed tomography (CT) scan of the thoracic and abdominal organs was performed. The examination reveals numerous round, hypervascular metastatic lesions distributed throughout both lobes of the liver. Multiple bilateral pulmonary metastases are also present, accompanied by atelectasis of the middle lobe. In addition, osteolytic metastatic lesions are identified within the visualized portions of the skeleton.

Table 1
Molecular-genetic results of primary and recurrent GBM.

	Primary tumor	Recurrent tumor
Single nucleotide variant (SNV)	(AF % for SNVs / copy number for CNVs)	(AF % for SNVs / copy number for CNVs)
TERT (NM_198253.3)	c.-124C>T (12.8%)	c.-124C>T (44.4%)
ARID1A (NM_006015.6)	c.1669 C>G, p.(Q557E) (58.3%)	c.1669 C>G, p.(Q557E) (51.4%)
PTEN (NM_000314.8)	c.227_228del, p.(Y76*) (65.9%)	c.227_228del, p.(Y76*) (43.9%)
RB1 (NM_000321.3)	c.935del, p.(P312Qfs*20) (63.7)	c.935del, p.(P312Qfs*20) (43.7)
TP53 (NM_000546.6)	c.584 T > C, p.(I195T) (64.6%)	c.584 T > C, p.(I195T) (54.0%)
NF1 (NM_001042492.3)	c.7314 C>A, p.(Y2438*) (62.9%)	c.7314 C>A, p.(Y2438*) (55.8%)
Copy number variants (CNVs)		
amplification/gain	*EGFR* (4.5x) *PMS2* (4.2x) *CDK6* (3.8x) *MET* (3.9x) *BRAF* (4.4x)	none detected
deletion/loss	none detected	none detected
Fusions	none detected	none detected
Chromosomal alterations		
amplification/gain	3p arm (2.5–2.8x; borderline) chromosome 7 (4.0–4.6x) chromosome 9 (2.5–3.0x; borderline)	14q arm (2.6–2.9, borderline)
deletion/loss	none detected	none detected
Tumor mutation burden	8.0 variants / Mb	8.0 variants / Mb
MGMT promotor methylation	No.	NA
DNA Methylation profile	Mesenchymal	NA

significant decrease in viability was observed in both GBM and GSC cell lines after 1 week (Fig. 4A) with higher concentrations of TRA, with GSC cells showing greater sensitivity and reduced viability even at lower TRA concentration of 50 nM. No significant effect of GAL or VS−4718 was observed during this treatment period (Fig. S4). Combinations of TRA with 100 μM TMZ were tested to assess any potential impact of TMZ. Results showed that TMZ alone has no significant effect on cell viability, confirming that the reduction in viability is primarily due to TRA (Fig. 4B). For the 48 h treatment, a significant decrease in viability was seen only in the GBM cell line with a final concentration of 50 nM TRA (Fig. S3A). Combinations of GAL and VS−4718 with TMZ were performed to observe any potential impact of TMZ and the combination of inhibitors with TMZ after one week. Results showed no significant influence on cell viability (Fig. S5).

3. Cerebral organoids established by improved protocol of their maintenance and long-term survival are not affected by trametinib and temozolomide

To investigate the effect of TRA in a more complex environment, CO and CO-GSC assembloids were established from iPSCs and NIB315 patient-derived GSCs. COs were generated following a published protocol [21], with modifications introduced to enhance long-term survival and maturation (Fig. 5A). Using a ClinoStar rotating chamber bioreactor system (Celvivo), COs were maintained for over three months, at which point only 11% of cells within the COs were identified as non-viable (Fig. 5C). Cerebral architecture, self-organization, and cellular differentiation were evaluated by immunofluorescence staining at the time of CO-GSC assembly (40-day-old COs) and by flow cytometry after three months in ClinoStar. At 40 days *in vitro*, COs were immunopositive for the neural stem cell marker SOX2, the differentiated neuronal marker TUJ1, the late immature neuronal markers NeuN and MAP2, the proliferation marker Ki−67, and the hypoxia marker CA9 at some regions. At this developmental stage, COs were negative for CD133 and did not express the astrocyte markers EAAT1 and GFAP. COs generated with this protocol expressed the forebrain/midbrain marker OTX2 and exhibited ventricular zone-like neuroepithelial rosettes immunopositive for the dorsal forebrain marker PAX6 (Fig. 5B). After three months in culture, COs retain neural stem cells (SOX2) and early differentiating neurons (NeuroD1, TUJ1), while also containing more mature neurons (NeuN, MAP2), and forebrain identity markers (OTX2 and PAX6), proliferative cells (Ki67) and some hypoxic regions (CA9). Additionally, they also showed appropriate glial differentiation, as evidenced by expression of astrocyte markers (EAAT1 and GFAP) (Fig. 5C, Fig S6).

Using newly established COs, which provide a physiologically relevant environment for evaluating drug toxicity, we further tested the selectivity and potential side effects of TRA on COs. We confirmed that TRA, even at the highest concentration and in combination with standard therapy, had no significant effect on cell viability or cytotoxicity after 48 h (Fig. S7A) and after 1 week of treatment (Fig. S7B).

4. Trametinib in combination with temozolomide inhibits GBM cell invasion into COs

As TRA showed the strongest inhibitory effect in cell viability and cytotoxicity assays, we further assessed its impact on 3D cell invasion. First, we performed a 3D invasion assay in Matrigel after one week of treatment of NIB315 GSC spheroids (Fig. S8). TMZ alone inhibited invasion of NIB315 GSCs, but TRA alone or in combination with TMZ produces stronger inhibition, which appeared to be driven primarily by the effect of TRA (Fig. S9).

To evaluate the effect of TRA in a more physiologically relevant environment, we used the CO-NIB315 GSC assembloid model, which recapitulates the three-dimensional architecture of the tumor-brain interface and allows quantification of GBM cell invasion into CO tissue. Invasion in the CO-NIB315 GSC assembloid model was significantly reduced after combined TRA and TMZ treatment, as quantified by CD133-positive area normalized to the total assembloid area, while a trend towards reduced invasion was also observed after TRA monotherapy (Fig. 6C, D). Along with the invasion assay, we observed that cell cytotoxicity was not affected by TRA or TRA + TMZ at the concentrations used, as measured with the LDH-Glo cytotoxicity assay (Fig. 6B).

4. Discussion

We report a rare case of GBM with extraneural metastases involving the liver, lungs, and skeletal system. The 47-year-old female patient had an overall survival of 12 months from diagnosis to death, which falls within the previously reported survival range of 7.5–26 months for metastatic GBM. The interval between initial diagnosis and the emergence of metastatic disease was 10 months, also consistent with published data indicating a mean or median interval of 10–26 months. It is important to recognize that studies conducted prior to the 2021 WHO classification may have included IDH-mutant tumors, which are now classified separately and are associated with a more favorable prognosis, potentially influencing earlier survival estimates. [24]. Despite multiple therapeutic attempts, no consensus exists regarding optimal treatment for metastatic GBM. Systemic chemotherapy—regardless of the specific agent—remains the only intervention shown to significantly prolong overall survival in this patient group [25]. A deeper understanding of the molecular and biological features of metastatic GBM is therefore essential for developing tailored therapeutic strategies.

Comprehensive histopathological and molecular profiling of the tumor biopsies revealed an unmethylated MGMT promoter and several clinically relevant genetic alterations. A pathogenic *TERT* promoter mutation was identified. *TERT* encodes a catalytic subunit of the telomerase complex, and TERT promoter mutations are common in GBM, occurring in 55–80% of cases [26,27]. These mutations have been

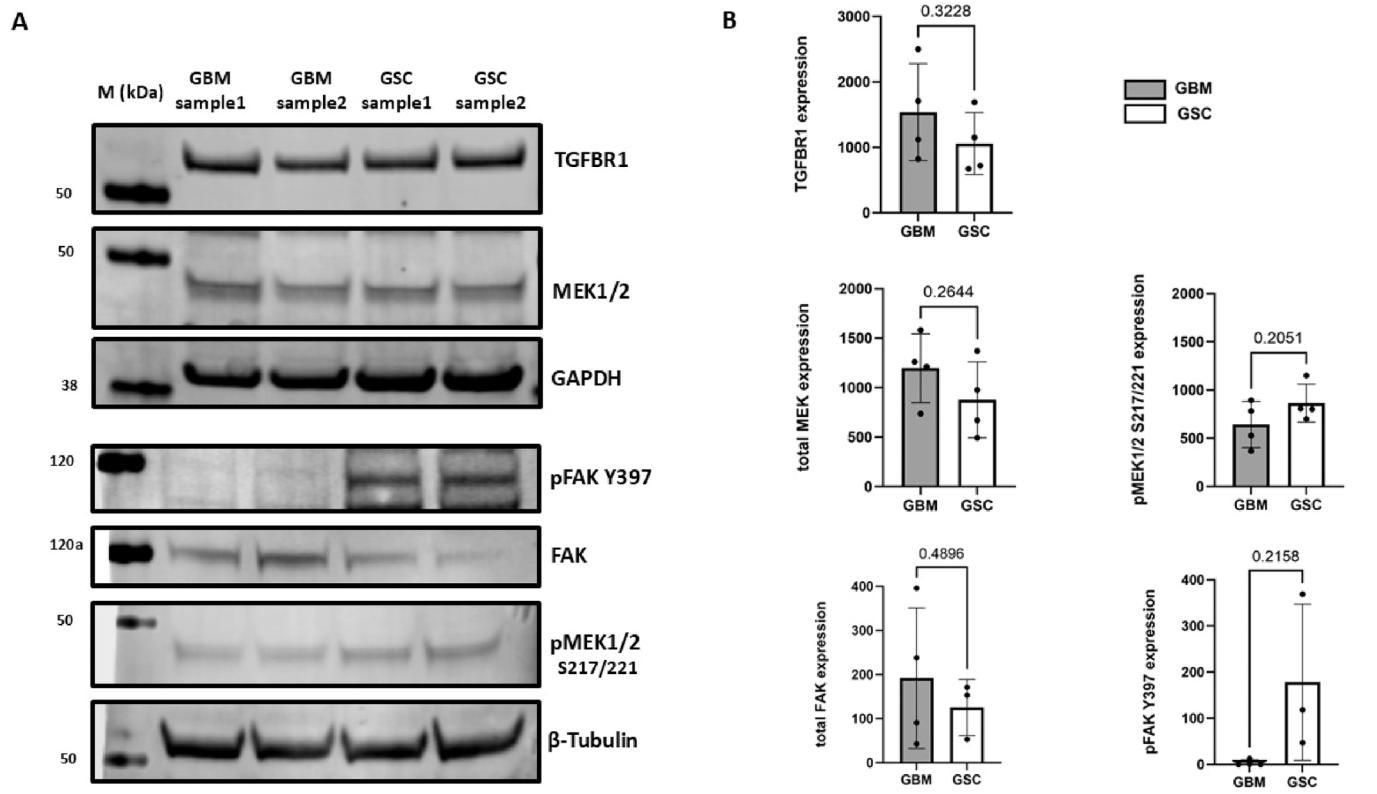

Fig. 3. Western blot confirmation of expression of targeted proteins. (A) TGFBR1, MEK1/2, pMEK1/2, FAK, and pFAK were analyzed in two biological samples of GBM and GSC cells and detected by fluorescence on Immobilon®-FL PVDF Membrane. Equal protein loading is shown with internal controls β-Tubulin and GAPDH. (B) Quantification summary of western blots was prepared with Empiria Studio 3.3 software (LICORbio™). Error bars represent means ± SEM, statistical analysis using Welch's *t*-test.

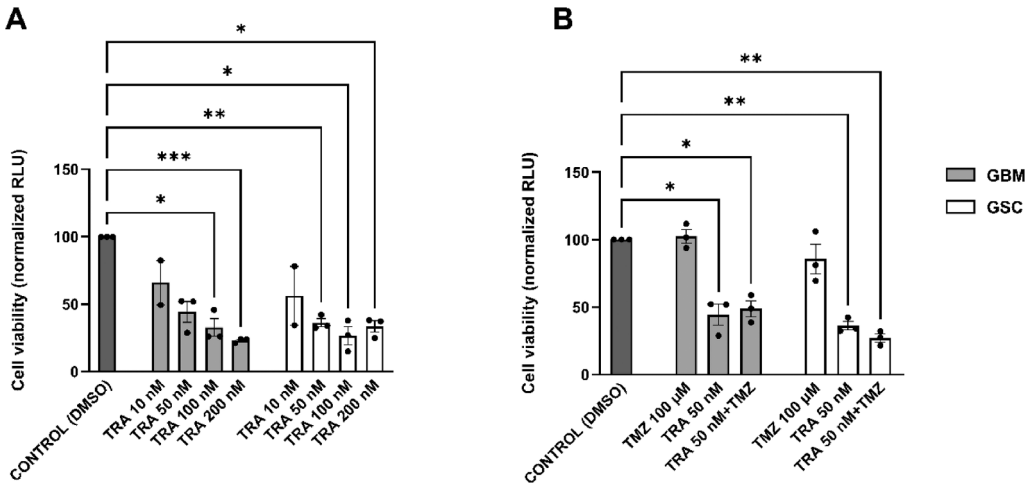

Fig. 4. Cell viability of GBM and GSC cell lines after 1 week treatment with trametinib (TRA) and its combination with TMZ. (A) Cell viability of GBM and GSC cell lines after 1 week of treatment with TRA. (B) Observed cell viability of GBM and GSC cell lines after 1 week treatment with a combination of TMZ and the inhibitor TRA. Cell viability was assessed after 7 days using the CellTiter Glo® 3D Viability Assay, and luminescence was measured on Luminometer Synergy HTX. All data were normalized to DMSO. Quantification was performed using GraphPad Prism 10, with statistical analysis by one-way ANOVA. Error bars represent means ± SEM; significance is indicated as * for $p < 0.05$, ** for $p < 0.01$, and *** for $p < 0.001$. The values of inhibitors on the x-axis represent the final concentrations of the treatment. For TMZ combinations (B), the final TMZ concentration was 100 µM, ($n = 3$).

already associated with metastatic GBM [3]. Several tumor suppressor genes showed inactivating alterations, including, *RB1, TP53, PTEN* and *NF1*, all present at high allele frequencies, indicating clonal events. Alterations in *RB1, TP53, PTEN* and *NF1* have previously been linked to metastatic GBM in a cohort of 10 patients with extraneural spread [3]. A missense variant in ARID1A was also detected; ARID1A mutations promote genomic instability through impaired mismatch repair and have been already reported in metastatic GBM [28,29]. Copy-number analysis of the primary tumor revealed high-level amplifications on chromosome 7 involving *EGFR, MET, CDK6, BRAF,* and *PMS2*. *EGFR* amplification has been associated with metastatic GBM and correlates positively with *TERT* promoter mutations [27]. *MET* and *CDK6*

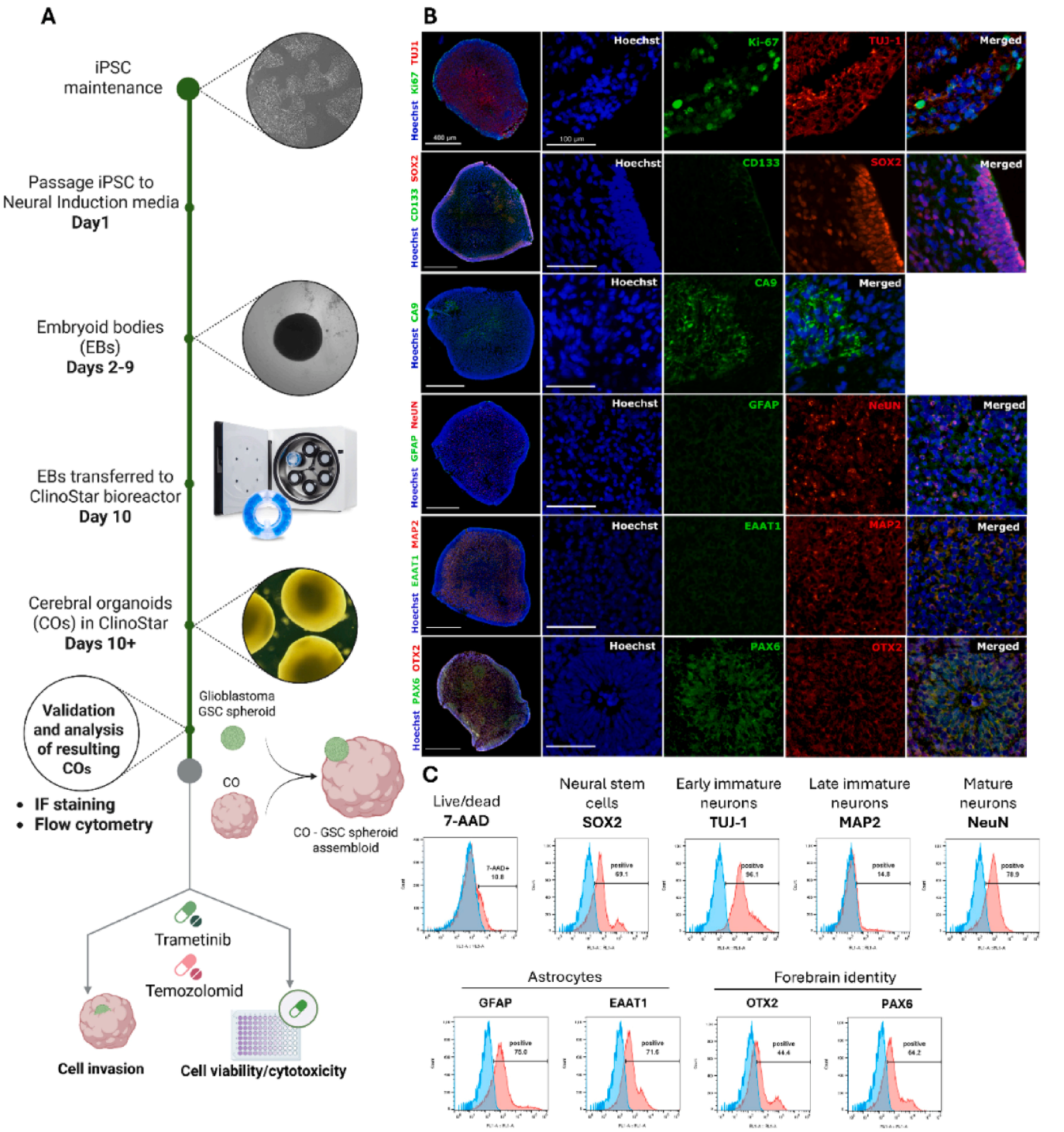

Fig. 5. CO generation, characterization, assembloid formation, and evaluation of GBM cell invasion and cytotoxicity. (A) Schematic overview of the workflow for generating COs and GBM assembloids. Human induced pluripotent stem cells (iPSCs) were differentiated into embryoid bodies (EBs) and maintained in static culture for 10 days. EBs were subsequently transferred to a ClinoStar bioreactor to promote CO formation and long-term maturation. Following validation of the resulting COs, assembloids were created by integrating GSC spheroids to assess treatment effects on GBM cell invasion and cytotoxicity. (B) Immunofluorescent characterization of 40-day-old COs. Organoids contained proliferative cells (Ki-67, green), early immature neurons (TUJ1, red), neural stem/progenitor cells (SOX2, red), and late immature and mature neurons (MAP2 and NeuN, both red). COs expressed the forebrain/midbrain marker OTX2 and dorsal forebrain marker PAX6 and were negative for CD133 and the astrocyte markers EAAT1 and GFAP. Hypoxic regions were detected using CA9 (green). Scale bars: 400 μm (overview images) and 100 μm (insets). C) Flow cytometry validation of 3-month-old COs. A small fraction of dead cells in COs was detected by flow cytometry using 7-AAD staining. COs express markers of neural stem cells (SOX2), early immature neurons (TUJ1) and mature neurons (NeuN), astrocytes (EAAT1 and GFAP), and forebrain identity (OTX2 and PAX6).

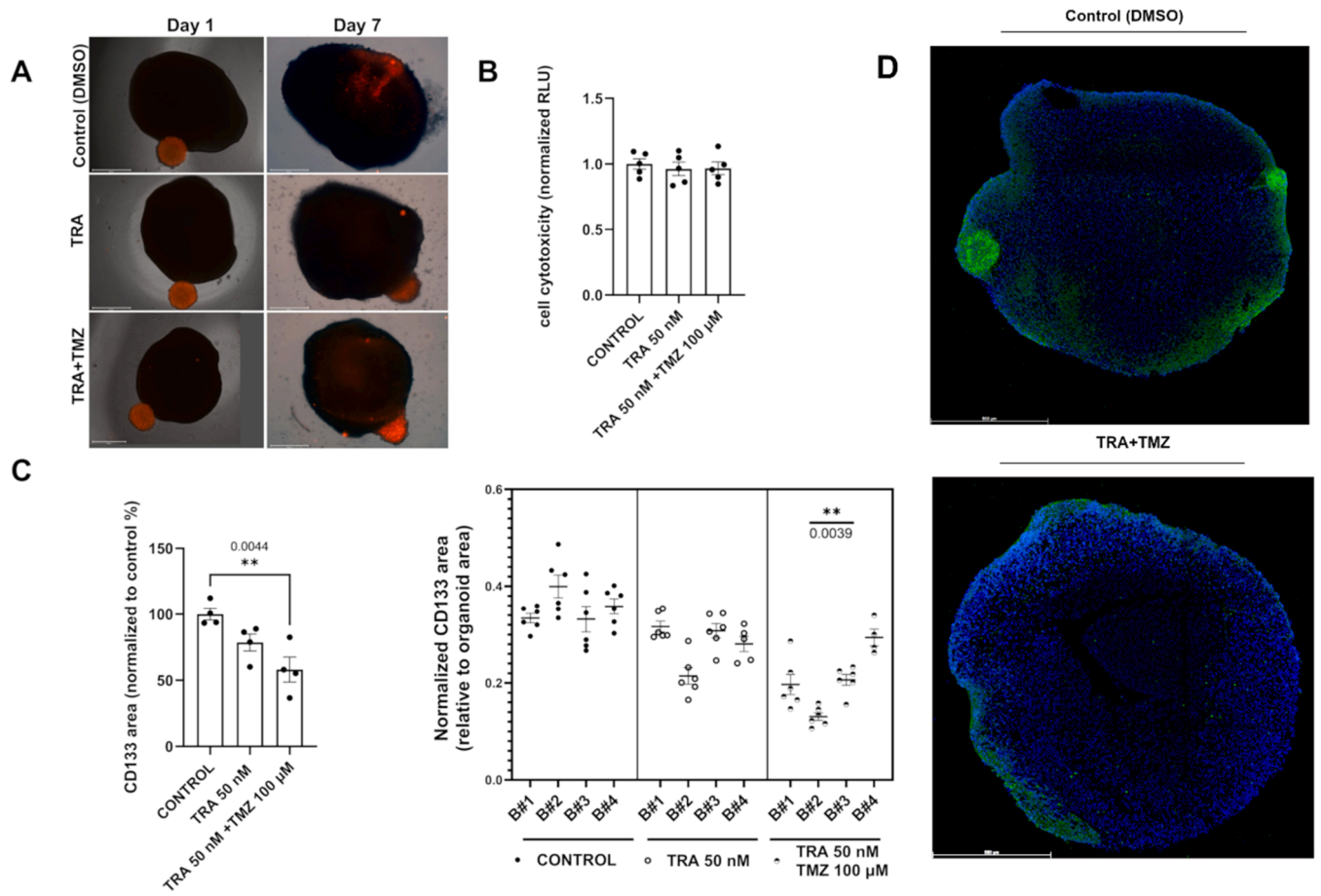

Fig. 6. Impact of trametinib (TRA) on tumor cell invasion. A) Representative images of the cerebral organoid (CO) and NIB315 GSC spheroid assembloids on day 1 and day 7 for control, TRA-treated and TRA-TMZ-treated conditions. COs were co-cultured with NIB315 GSC spheroids to generate assembloids, and brightfield and fluorescence images were acquired immediately after assembly (day 1) and after 7 days in culture to visualize spheroid attachment and spreading in all treatment groups. Scale bar: 650 µm. B) LDH-Glo cytotoxicity assay of cells treated with TRA or TRA + TMZ at the indicated concentrations after 1 week. Data represent mean ±SEM of n = 5 independent CO-NIB315 GSC assembloids. C) Invasion area (CD133 + area normalized to the total assembloid area) in the CO-NIB315 GSC assembloid model treated with TRA or TRA + TMZ at the indicated concentrations after 1 week. Four CO assembloids per condition were used as biological replicates. For each biological replicate, six consecutive sections were analyzed as technical replicates. The left graph summarizes all technical replicates (mean± SEM, ordinary one-way ANOVA with Dunnett's multiple comparisons test). All individual data points are additionally shown in a nested graph (mean ± SEM, nested one-way ANOVA with Dunnett's multiple comparisons test.) D) Representative confocal images of the CD133-positive area in control and combined TRA + TMZ treated assembloids, showing a visibly smaller CD133-positive area under combined treatment compared to control. Scale bars 500 µm. *TRA-trametinib, TMZ-temozolomide.

amplification, together with *TERT* promoter mutation, have been reported in GBM with scalp and lung metastasis [30]. *PMS2*, a mismatch-repair gene, has not previously been linked to metastatic GBM, although its amplification has been implicated in brain metastasis from lung cancer [31]. Notably, *PMS2* was also identified among genes expressed in circulating tumor cells from peripheral blood of GBM patients, suggesting a potential role in aggressive and disseminating GBM [4]. The recurrent tumor biopsy retained the core mutational profile of the primary tumor, supporting clonal continuity. However, it exhibited a marked reduction in copy-number alterations, including the loss of chromosome 7 amplifications. This may reflect clonal selection, genomic evolution under treatment pressure, or technical differences related to tumor purity or sampling. The latter is unlikely, as both samples were enriched using a 0.6-mm punch needle and contained approximately 80% viable tumor cells. Overall, the findings support tumor progression from a common ancestral clone, with divergence primarily at the level of copy-number alterations rather than point mutations.

Large-scale molecular profiling efforts have identified several GBM subtypes [32,33]; however, although DNA methylation–based classifications partially overlap with transcriptomic subclasses, they do not fully align with RNA-based groups or with proteogenomic and metabolomic tumor landscapes [34,35]. To date, these extensive molecular subclassification systems have not translated into meaningful clinical applications, underscoring the need for further studies to clarify their potential role in patient management. Genome-wide DNA methylation profiling has emerged as a powerful tool for accurate molecular classification of CNS tumors and enables further stratification of GBM into methylation subclasses such as RTK I, RTK II, and mesenchymal (MES). MES methylation subclass is characterized by increased tumor-infiltrating lymphocytes, but no recurrent mutations are specifically associated with this subclass [36]. The primary tumor in our case belonged to the MES methylation subclass, which has not previously been linked to GBM metastasis. Further studies are needed to clarify whether MES methylation subclass influences metastatic potential.

Genetic alterations found in our case drive growth signaling, cell cycle, genomic instability and invasion, which, when combined, are likely to have a collaborative effect maintaining tumor growth and spread [37]. *EGFR, MET,* and *BRAF* amplification, together with *NF1* mutation, activate signaling cascades such as RAS/RAF/MEK/ERK (MAPK) and FAK, which are implicated in tumor growth, therapy resistance, and dissemination [28,37–42]. However, based on

histopathological and molecular analyses of the recurrent tumor, the recurrent lesion was less dependent on chromosome 7-associated receptor tyrosine kinase signaling and prompted us to focus on downstream pathways with evidence of persistent activation. TGF-β signaling plays an oncogenic role in high-grade glioma by promoting GSC growth, activating MAPK signaling pathway, enhancing resistance to TMZ and invasion [43]. Consistent with these observations, the MAPK and TGF-β pathways were upregulated in patient-derived cancer cells from the recurrent tumor, whereas phosphorylated FAK was expressed at low levels in serum-grown GBM cells. These findings provided the rationale for prioritizing MEK-targeted therapy in our functional studies.

In addition to primary cancer cell cultures, we established personalized tumor models using assembloids composed of cortical organoids (COs),a human-relevant system that differs from traditional animal models [44], which are unable to replicate the intricate architecture and functionality of the human brain, and patient-derived GSCs (hybrid organoids) [19]. These models enabled us to evaluate drug selectivity and anti-tumor efficacy in a microenvironment that mimics human brain architecture. We upgraded the CO generation protocol based on published methods [20] and, to our knowledge, this is the first article report using the Celvivo ClinoStar rotating chamber system for long-term CO differentiation and maintenance. This approach supports reproducible, viable COs for up to three months by reducing fluid flow shear stress and eliminating ECM components—both critical factors that influence morphogenesis as well as organoid variability, and differentiation [45–47].

In the context of targeted therapies, tumor organoids can support both (pre)clinical studies and drug discovery pipelines. Assembloids between COs and GSCs can facilitate the research of cancer cell invasion and growth in interaction with healthy human brain and lead the development of personal anti-invasive strategies. Using these personalized tumor avatars, we demonstrated that TRA in combination with TMZ inhibited GSC invasion. Similar anti-invasive effects of TRA have been reported in GBM *in vitro* models [48]. Interestingly, an opposite effect—enhanced invasion following TRA treatment—was observed in a study by Furqan et al. [49] using a similar 3D spheroid invasion assay. This discrepancy likely reflects GBM heterogeneity and the use of different cell models.

We confirmed that TRA exhibited selective toxicity toward cancer cells isolated from a tumor biopsy of this proof-of-concept evidence study, consistent with clinical observations in pediatric gliomas, where MEK1/2 inhibition has shown efficacy and safety [50]. This suggests that MEK pathway targeting may be feasible in brain tumors without excessive toxicity. Trametinib reduced viability and invasion in both GBM and GSC cultures, indicating activity against therapy-resistant and aggressive cancer stem cell populations [51,52]. This may help counteract rapid intracranial and extraneural spread and improve responsiveness to standard therapies. Importantly, we demonstrated that MEK inhibition is effective in GBM lacking *BRAF V600E* mutation [11].

NF1 deficiency may be a key driver of TRA sensitivity in this case, as loss of neurofibromin leads to hyperactivation of RAS and downstream MAPK signaling. Numerous studies have shown the efficacy of MEK inhibitors in NF1-deficient tumors [53]. Furthermore, recent integrative analyses of large genomic, transcriptomic, proteogenomic, and metabolomic GBM datasets identified MAPK inhibitors—including TRA—as top candidates for reversing NF1-altered molecular signatures, pointing out MAPK inhibitors as top candidate drugs for GBMs with NF1 alterations [34].

In summary, metastatic GBM remains poorly understood, and comprehensive preclinical and clinical studies for this GBM patient groups are scarce. Through detailed molecular profiling, we identified several molecular features—including tumor suppressor *NF1, TP53, PTEN, and RB1* alterations, MES methylation subclass and MAPK pathway activation—that likely contributed to tumor aggressiveness and extraneural metastases. By developing personalized tumor models that recapitulate patient-specific tumor biology and the human brain microenvironment, we identified TRA as a promising candidate capable of selectively inhibiting the viability and invasion of highly aggressive GBM cells within this individualized tumor avatar system. MEK inhibition may help counteract rapid tumor spread and improve responsiveness to standard chemotherapy. These findings provide proof-of-concept evidence for the potential utility of MEK inhibition in this specific metastatic GBM case but do not establish TRA as a broadly applicable therapeutic strategy for metastatic GBM. This work underscores the complexity of metastatic GBM and highlights the need for continued research, including validation in additional models and clinical studies, to evaluate the generalizability of these findings and support the development of targeted therapeutic approaches.

Author contributions statement

M.N.,M.S.V., B.M. and B.B.V. designed the study. M.N., B.M., Š.K., T. K.M., A.H., S.K.G. and P.Ž performed wet lab experiments and analyzed and interpreted data. M.S.V, A.P., A.M., A.Z., M.J., M.B., and B.P. provided clinical data and samples and analyzed the data. B.B.V., M.N., B. M., wrote the first draft of the manuscript. All authors reviewed and approved the submitted manuscript.

CRediT authorship contribution statement

Bernarda Majc: Writing – original draft, Visualization, Validation, Methodology, Formal analysis, Data curation. **Matic Bošnjak:** Methodology, Investigation, Formal analysis, Data curation. **Borut Prestor:** Supervision, Resources, Methodology, Investigation. **Marija Skoblar Vidmar:** Visualization, Investigation, Funding acquisition, Data curation, Conceptualization. **Barbara Breznik Vittori:** Writing – original draft, Supervision, Project administration, Methodology, Investigation, Funding acquisition, Data curation, Conceptualization. **Špela Kladnik:** Formal analysis. **Tina Kolenc Milavec:** Formal analysis. **Anamarija Habič:** Methodology, Formal analysis. **Pia Žižek:** Formal analysis. **Andrej Porčnik:** Methodology, Investigation, Data curation. **Alenka Matjašič:** Methodology, Investigation, Formal analysis, Data curation. **Andrej Zupan:** Methodology, Investigation, Formal analysis, Data curation. **Galun Simona:** Formal analysis. **Metka Novak:** Writing – review & editing, Writing – original draft, Validation, Supervision, Methodology, Investigation, Funding acquisition, Conceptualization. **Miha Jerala:** Methodology, Investigation, Formal analysis, Data curation.

Ethics approval and consent to participate

Approval by the National Medical Ethics Committee of the Republic of Slovenia was obtained (number 0120–190/2018–2711–46) for collecting and processing tumor tissue material, performing research on patient's material, and using the corresponding personal data. Patient or their authorized representatives signed the informed consent form in accordance with the Declaration of Helsinki.

Consent for publication

Patient or their authorized representatives signed the informed consent form in accordance with the Declaration of Helsinki that includes the statemenet of consent for publication.

Funding

This study was supported by the Slovenian Research and Innovation Agency (programme and research grants P1–0245, J3–4504, NC−25002, N3–0394, L3–3176, BI-TR/25–27–003, J7–70250, Z3–70129, J2–70099 and young researcher grant to AH and SKG), European Union's projects CutCancer 101079113 and GenomeMET 22HLT06.

Declaration of Competing Interest

The authors declare that they have no financial, commercial, personal, or academic conflicts of interest that could have influenced the research, analysis, or conclusions presented in this manuscript. No external entity had any role in the study design, data collection, interpretation, or the decision to submit this work for publication.

Acknowledgments

We acknowledge the support of the entire team at the Institute of Pathology, Faculty of Medicine, University of Ljubljana, Slovenia, whose consistent expertise and care in preparing our FFPE slides greatly contributes to our work. We acknowledge the support of COST actions IMMUNO-model CA21135 and Net4Brain CA22103.

Appendix A. Supporting information

Supplementary data associated with this article can be found in the online version at doi:10.1016/j.biopha.2026.119832.

Data availability

The datasets generated and analyzed during this study are available in the BioImages Database BioStudies under accession number S-BIAD3075 https://www.ebi.ac.uk/biostudies/bioimages/studies/S-BIAD3075.

References

[1] S.P. Weathers, et al., Improved overall survival in an anti-PD-L1 treated cohort of newly diagnosed glioblastoma patients is associated with distinct immune, mutation, and gut microbiome features: a single arm prospective phase I/II trial, Nat. Commun. 2025 16 (1 16) (2025) 3950.
[2] W. Wei, et al., Single-cell phosphoproteomics resolves adaptive signaling dynamics and informs targeted combination therapy in glioblastoma, Cancer Cell. 29 (2016) 563–573.
[3] E.K. Noch, S.F. Sait, S. Farooq, T.M. Trippett, A.M. Miller, A case series of extraneural metastatic glioblastoma at Memorial Sloan Kettering Cancer Center, Neurooncol. Pract. 8 (2021) 325–336.
[4] I. Krol, et al., Detection of circulating tumour cell clusters in human glioblastoma, Br. J. Cancer 2018 119 (4 119) (2018) 487–491.
[5] J. Behnan, G. Finocchiaro, G. Hanna, The landscape of the mesenchymal signature in brain tumours, Brain 142 (2019) 847–866.
[6] J.P. Sullivan, et al., Brain tumor cells in circulation are enriched for mesenchymal gene expression, Cancer Discov. 4 (2014) 1299–1309.
[7] J.V. Joseph, et al., TGF-β promotes microtube formation in glioblastoma through thrombospondin 1, Neuro. Oncol. 24 (2022) 541–553.
[8] S. Peñuelas, et al., TGF-β increases glioma-initiating cell self-renewal through the induction of LIF in human glioblastoma, Cancer Cell. 15 (2009) 315–327.
[9] N.F. Brown, et al., A study of the focal adhesion kinase inhibitor GSK2256098 in patients with recurrent glioblastoma with evaluation of tumor penetration of [11C] GSK2256098, Neuro. Oncol. 20 (2018) 1634–1642.
[10] M. Houweling, et al., Radio-sensitizing effect of MEK inhibition in glioblastoma in vitro and in vivo, J. Cancer Res. Clin. Oncol. 149 (2023) 297–305.
[11] J. Steininger, et al., Efficacy of BRAF/MEK-inhibitor therapy for epithelioid glioblastoma with a novel BRAFV600 mutation, Acta Neuropathol. Commun. 12 (2024) 124.
[12] A.E. Armstrong, A.J. Belzberg, J.R. Crawford, A.C. Hirbe, Z.J. Wang, Treatment decisions and the use of MEK inhibitors for children with neurofibromatosis type 1-related plexiform neurofibromas, BMC Cancer 23 (2023) 553.
[13] J. Ortiz-Rivera, R. Nuñez, Y. Kucheryavykh, L. Kucheryavykh, The PYK2 inhibitor PF-562271 enhances the effect of temozolomide on tumor growth in a C57Bl/6-Gl261 mouse glioma model, J. Neurooncol. 161 (2023) 593–604.
[14] N.F. Brown, et al., A study of the focal adhesion kinase inhibitor GSK2256098 in patients with recurrent glioblastoma with evaluation of tumor penetration of [11C] GSK2256098, Neuro. Oncol. 20 (2018) 1634–1642.
[15] A.A. Brandes, et al., A Phase II randomized study of galunisertib monotherapy or galunisertib plus lomustine compared with lomustine monotherapy in patients with recurrent glioblastoma, Neuro. Oncol. 18 (2016) 1146–1156.
[16] M. Logun, et al., Patient-derived glioblastoma organoids as real-time avatars for assessing responses to clinical CAR-T cell therapy, Cell. Stem Cell. 32 (2025) 181–190.e4.
[17] F. Jacob, et al., A patient-derived glioblastoma organoid model and biobank recapitulates inter- and intra-tumoral heterogeneity, Cell 180 (2020) 188–204.e22.
[18] B. Majc, et al., Patient-derived tumor organoids mimic treatment-induced DNA damage response in glioblastoma, iScience 27 (2024).
[19] M. de Lucas Sanz, S.P. Niclou, A. Golebiewska, Modelling brain tumours with organoids: towards precision medicine in neuro-oncology, Nat. Rev. Neurol. 2026 119 (2026), https://doi.org/10.1038/s41582-026-01190-2.
[20] C. Anastasaki, A.F. Wilson, A.S. Chen, M.L. Wegscheid, D.H. Gutmann, Generation of human induced pluripotent stem cell-derived cerebral organoids for cellular and molecular characterization, STAR Protoc. 3 (2022) 101173.
[21] M. Novak, et al., The Slovenian translational platform GlioBank for brain tumor research: Identification of molecular signatures of glioblastoma progression, vdaf015, Neurooncol. Adv. 7 (2025). vdaf015.
[22] D.N. Louis, et al., The 2021 WHO classification of tumors of the central nervous system: a summary, Neuro. Oncol. 23 (2021) 1231–1251.
[23] B. Majc, M. Novak, Trametinib in combination with temozolomide inhibits GBM cell invasion into cerebral organoids, BioImage Arch. Database Prepr. (2026), https://doi.org/10.6019/S-BIAD3075.
[24] E.M. Taule, et al., Breaking boundaries: a rare case of glioblastoma with uncommon extraneural metastases: a case report and literature review, Brain Spine 4 (2024) 103927.
[25] G. Kalokhe, et al., Metastatic glioblastoma: case presentations and a review of the literature, J. Neurooncol. 107 (2012) 21–27.
[26] N. Olympios, et al., TERT promoter alterations in glioblastoma: a systematic review, 13, Cancers 2021 13 (2021) 1–19.
[27] N. Nonoguchi, et al., TERT promoter mutations in primary and secondary glioblastomas, Acta Neuropathol. 126 (2013) 931–937.
[28] J. Shen, et al., ARID1A deficiency promotes mutability and potentiates therapeutic antitumor immunity unleashed by immune checkpoint blockade, Nat. Med. 2018 24 (5 24) (2018) 556–562.
[29] M. Umphlett, et al., Widely metastatic glioblastoma with BRCA1 and ARID1A mutations: a case report, BMC Cancer 20 (2020) 47.
[30] Y. Tsukamoto, et al., Rapidly progressive scalp and lung metastases with fatal pneumothorax in glioblastoma, IDH-wildtype, with MET and CDK6 amplifications: a case report of clinical course and postmortem autopsy, including genetic analysis, Brain Tumor Pathol. 42 (2025) 94–103.
[31] J. Chen, et al., PMS2 amplification contributes brain metastasis from lung cancer, Biol. Proced. Online 26 (2024) 12.
[32] R.G.W. Verhaak, et al., Integrated genomic analysis identifies clinically relevant subtypes of glioblastoma characterized by abnormalities in PDGFRA, IDH1, EGFR, and NF1, Cancer Cell. 17 (2010) 98–110.
[33] C.W. Brennan, et al., The somatic genomic landscape of glioblastoma, Cell 155 (2013) 462.
[34] L.B. Wang, et al., Proteogenomic and metabolomic characterization of human glioblastoma, e20, Cancer Cell. 39 (2021) 509–528. e20.
[35] R. Drexler, et al., DNA methylation subclasses predict the benefit from gross total tumor resection in IDH-wildtype glioblastoma patients, Neuro. Oncol. 25 (2023) 315–325.
[36] R. Drexler, et al., Temporal change of DNA methylation subclasses between matched newly diagnosed and recurrent glioblastoma, Acta Neuropathol. 147 (2024) 21.
[37] A. Pouyan, et al., Glioblastoma multiforme: insights into pathogenesis, key signaling pathways, and therapeutic strategies, Mol. Cancer 2025 24 (1 24) (2025) 58.
[38] H. Davies, et al., Mutations of the BRAF gene in human cancer, *6892* 417, Nature 2002 417 (2002) 949–954.
[39] A.E. Armstrong, A.J. Belzberg, J.R. Crawford, A.C. Hirbe, Z.J. Wang, Treatment decisions and the use of MEK inhibitors for children with neurofibromatosis type 1-related plexiform neurofibromas, BMC Cancer 23 (2023) 553.
[40] F. Cheng, D. Guo, MET in glioma: signaling pathways and targeted therapies, J. Exp. Clin. Cancer Res. 38 (2019) 270.
[41] H.H. Chuang, et al., FAK in cancer: from mechanisms to therapeutic strategies, Int. J. Mol. Sci. 2022 23 (23) (2022).
[42] T.H. Chen, P.C. Chan, C.L. Chen, H.C. Chen, Phosphorylation of focal adhesion kinase on tyrosine 194 by Met leads to its activation through relief of autoinhibition, Oncogene 2011 30 (2 30) (2010) 153–166.
[43] I. Golán-Cancela, L. Caja, The TGF-β Family in Glioblastoma, Int. J. Mol. Sci. 2024 25 (25) (2024).
[44] R. Coronel, R. González-Sastre, P. Mateos-Martínez, et al., Human cerebral organoids: complex, versatile, and human-relevant models of neural development and brain diseases, Neural Regen. Res. 21 (3) (2026) 837–854.
[45] G. Aiello, et al., Increased reproducibility of brain organoids through controlled fluid dynamics, EMBO Rep. 26 (2025) 6209–6239.
[46] P. Saglam-Metiner, et al., Spatio-temporal dynamics enhance cellular diversity, neuronal function and further maturation of human cerebral organoids, 6, Commun. Biol. 2023 6 (1) (2023) 173.
[47] A. Jain, et al., Morphodynamics of human early brain organoid development, *8078* 644, Nature 2025 644 (2025) 1010–1019.
[48] A. Berberich, et al., Targeting resistance against the MDM2 inhibitor RG7388 in glioblastoma cells by the MEK inhibitor trametinib, Clin. Cancer Res. 25 (2019) 253–265.
[49] M. Furqan, et al., Drug combinations targeting FAK and MEK overcomes tumor heterogeneity in glioblastoma, Pharmaceutics 17 (2025).
[50] J. Fangusaro, et al., Selumetinib in paediatric patients with BRAF-aberrant or neurofibromatosis type 1-associated recurrent, refractory, or progressive low-grade glioma: a multicentre, phase 2 trial, Lancet Oncol. 20 (2019) 1011–1022.

[51] S. Khan, et al., Neuronal differentiation drives the antitumor activity of mitogen-activated protein kinase kinase (MEK) inhibition in glioblastoma, Neurooncol. Adv. 5 (2023) 1–15.
[52] B. Breznik, et al., Infiltrating natural killer cells bind, lyse and increase chemotherapy efficacy in glioblastoma stem-like tumorospheres, 5, Commun. Biol. 2022 5 (1) (2022) 436.
[53] A.E. Armstrong, A.J. Belzberg, J.R. Crawford, A.C. Hirbe, Z.J. Wang, Treatment decisions and the use of MEK inhibitors for children with neurofibromatosis type 1-related plexiform neurofibromas, BMC Cancer 23 (2023) 553.